Time-dependent Lattice Cross Sections and Line Ratios for Solar Wind Charge Exchange: Bare Ne Incident on Atomic H and He

S. J. Bromley ⬤, M. Pindzola ⬤, D. Bodewits ⬤, and M. R. Fogle ⬤
Department of Physics, Auburn University, Leach Science Center, Auburn, AL 36849, USA; sjb0068@auburn.edu
Received 2022 May 6; revised 2022 August 12; accepted 2022 August 13; published 2022 September 30

Abstract

Charge exchange (CX) between highly charged ions and neutrals within the geocorona and heliosphere introduces a problematic background for every X-ray observation. For H-like ions the ℓ states within each n shell are degenerate. The majority of CX spectral models rely on calculated n-resolved cross sections, and the distribution of ℓ states is assumed to follow one of several analytical expressions. Laboratory data to validate these distributions at solar wind velocities is not available. Explicitly velocity-dependent calculations of $n\ell$-resolved CX cross sections using the time-dependent lattice (TDL) method for Ne^{10+} incident on atomic H and He at 1–5 keV amu^{-1} are reported. The cross sections are incorporated into a radiative cascade model, and the influence of n- and $n\ell$-resolved cross sections on possibly diagnostic emission line ratios is investigated. Comparisons of the ℓ distribution extracted from the TDL cross sections to the predominantly used analytical distributions reveals a consensus among n and $n\ell$-resolved data at solar wind velocities, suggesting a statistical distribution is most appropriate for CX collisions involving atomic H. No consensus is found for atomic He targets, and the ℓ distribution extracted from $n\ell$-resolved cross sections appears most appropriate. Open questions related to CX are discussed with emphasis on experimental methods to resolve them. Spectral measurements at an electron beam ion trap facility are planned to benchmark the presented cross section data.

Unified Astronomy Thesaurus concepts: Charge exchange recombination (2062); Solar wind (1534)

1. Introduction

Charge exchange (CX) is a common collisional process at interfaces between hot, ionized gas and cold media, e.g., supernovae remnants, galaxy clusters, and more (Dennerl 2010). This process is not isolated to extrasolar sources. Solar wind interactions with Earth's geocorona and exosphere, whose CX emission varies as a function of both observing geometry and time, is present to some degree in every X-ray observation (Kuntz 2018). This CX emission is also prodigious as observed around comets, see, for example, Bonamente et al. (2021) or Bodewits et al. (2007). The net CX process can be expressed as

$$A^{q+} + B \rightarrow A^{(q-j)+} + B^{j+} + \gamma \qquad (1)$$
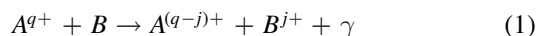
where ion A^{q+} (referred to as the projectile) captures j electrons from neutral B (the "target") into an excited state(s). Subsequent decays return the ion to the ground state, releasing photon(s) γ. To date, studies of CX have largely focused on single-electron capture (SEC; $j = 1$), particularly at the high energies (∼0.1–1.0 MeV) relevant for laboratory plasma environments, e.g., fusion plasma devices. For multielectron targets multielectron capture (MEC; $j > 1$) processes become possible, such as true double-electron capture or double-capture autoionization, but the exact contribution to the total cross section and the X-ray spectrum remains an open question (see, for example, Bodewits & Hoekstra 2007 or Bodewits & Hoekstra 2019).

For SEC with the simplest target (H), open questions remain. For bare ions undergoing CX to produce H-like ions,

the angular momentum ℓ states within each n shell are degenerate. Various computational approaches have previously been employed to compute either n or $n\ell$-resolved cross sections. Atomic orbital close coupling (AOCC; e.g., Fritsch & Lin 1991) solves the time-dependent Schrödinger equation for the two collision partners, each represented by atomic orbitals, and produces $n\ell$-resolved cross sections. At very low collision energies the quantum molecular orbital close coupling method (QMOCC; see e.g., Zygelman et al. 1992) explicitly treats the colliding system as a quasi-molecule. However, QMOCC calculations are computationally expensive and involve potentially many thousands of coupled channels. Rather, it is most common to utilize n-resolved data calculated with the computationally less-expensive multichannel Landau–Zener (MCLZ; Butler & Dalgarno 1980) method, which may be considered as an approximation of QMOCC. Classical methods such as classical-trajectory Monte Carlo (CTMC; Olson & Salop 1977) have also been employed, though the accuracy at lower collision velocities where quantum-mechanical efforts are important is unclear.

The post-CX ℓ distribution of capture states has a significant effect on the X-ray spectra and resulting line ratios (Beiersdorfer et al. 2001), and thus n-resolved cross sections must be used with some applied ℓ distribution. At low collision velocities of order 0.01–0.1 keV amu^{-1}, the so-called "low-energy" distribution is assumed,

$$W_{n\ell}^{le} = \frac{(2\ell + 1)[(n - \ell)!]^2}{(n + 1)!(n - 1 - \ell)!}, \qquad (2)$$

which favors population of p ($\ell = 1$) states (Janev et al. 1983). The second most common distribution is the statistical

distribution

$$W_{n\ell}^{st} = \frac{2\ell + 1}{n^2}, \qquad (3)$$

which is typically adopted at energies of order 10 keV amu^{-1} or higher (Janev et al. 1983). Two additional ℓ distributions are available in AtomDB (Foster & Heuer 2020) and KRONOS (Lyons et al. 2017), the separable distribution

$$W_{n\ell}^{\mathrm{sep}} = \frac{(2\ell + 1)}{q} \exp\left[\frac{-\ell(\ell + 1)}{q} \right] \qquad (4)$$

and the "modified low-energy" distribution

$$W_{n\ell}^{\mathrm{LowMod}} = \ell(\ell + 1)(2\ell + 1) \frac{(n - 1)!(n - 2)!}{(n + \ell)!(n - \ell - 1)!}, \qquad (5)$$

where the separable distribution depends on the initial ion charge, q, and the modified low-energy distribution yields 0 population of s ($\ell = 0$) states.

Currently, the KRONOS[1] database acts as an aggregator of theoretical CX cross section data, including both n- and $n\ell$-resolved data for numerous ion/neutral combinations, as well as codes for generating important line ratios from CX cross sections via cascade modeling. It is generally assumed that when both n and $n\ell$-resolved data are available, the more computationally expensive methods (e.g., AOCC, see discussion in KRONOS documentation) are preferred as they include quantum-mechanical effects and consider ℓ-dependent capture channels explicitly.

Fogle & Pindzola (2020) reported theoretical $n\ell$-resolved CX cross sections for collisions between bare Mg incident on atomic H and He at velocities of 1, 3, and 5 keV amu^{-1} calculated with the time-dependent lattice (TDL) method. Here we report on the use of the same TDL approach to calculate $n\ell$-resolved cross sections for bare Ne incident on atomic H and He at energies spanning 1–5 keV amu^{-1}. Bare Ne was chosen as its Lyman series is in the 1–1.5 keV bandpass which has been observed in different environments, including cometary atmospheres (Ewing et al. 2013) and the Earth's geocorona (Carter et al. 2010; Fujimoto et al. 2007), and has been invoked to explain X-ray emission from the North Polar Spur, an elongated region of extended X-ray emission approximately north of the Galactic center (Lallement 2009; Gu et al. 2017).

For energies between ∼0.1–10 keV amu^{-1}, which includes typical solar wind velocities of 300–1000 km s^{-1}, the low-energy ℓ distribution is commonly assumed for use with n-resolved data. The low-energy ℓ distribution has found good agreement with, e.g., X-ray spectra collected inside electron beam ion trap (EBIT) experiments, where the collision velocities are well below those of the solar wind. EBIT CX spectra are subject to additional complications as multielectron processes are anticipated to have large cross sections at the available energies. Laboratory studies with sufficient spectral resolution to validate computed ℓ-resolved CX cross sections at solar wind velocities are presently unavailable.

Using our $n\ell$-resolved cross sections and existing $n\ell$-resolved data in the literature, we investigated the spectral differences driven by explicit ℓ distributions inherent in, e.g., TDL data, and analytical ℓ distributions (Equations (2)–(5)). In

doing so, we aim to probe the validity of commonly assumed distributions at typical solar wind collision energies and enhance the scientific value of existing cross section data.

The remainder of this work is organized as follows. In Section 2, we discuss our theoretical methods for calculating the $n\ell$-resolved cross sections, fundamental atomic data for H-like Ne (lines and levels), and our X-ray cascade code. In Section 3, our cross section data are presented, and comparisons to the existing literature are discussed. Section 4 details the implications for X-ray spectroscopy and the use of ℓ distributions with n-resolved data by placing the work in the context of both existing and expected data needs for high-resolution X-ray spectroscopy. The work is summarized in Section 5.

2. Computational Methods

2.1. Charge Exchange Cross Sections

The TDL method has previously been used to investigate SEC between neutral atoms and Be^{4+} (Minami et al. 2006), C^{6+} (Pindzola & Fogle 2015), O^{8+} (Pindzola et al. 2018), and most recently bare Mg incident on atomic H and He at solar wind velocities (Fogle & Pindzola 2020). Specifics regarding the computational implementation of the TDL method are available in, e.g., Pindzola & Schultz (2008) and references therein. A brief overview of the method is provided here.

For bare-ion collisions with atoms the time-dependent Schrödinger equation, in the frame of reference of the stationary Ne^{10+} ion, is given in atomic units by:

$$i \frac{\partial P(x, y, z, t)}{\partial t} = \left(-\frac{1}{2} \nabla^2 - \frac{10.0}{r} \right) P(x, y, z, t) + W(x, y, z, t) P(x, y, z, t). \qquad (6)$$

The potential between the valence electron and the core of the neutral, $W(x, y, z, t)$, takes the form

$$W(x, y, z, t) = -\frac{1}{R(t)}, \qquad (7)$$

for atomic H, and a model potential for He is assumed as (Jain et al. 1987)

$$W(x, y, z, t) = -\frac{1}{R(t)} - \frac{[1 + 1.665R(t)]\exp[-3.36R(t)]}{R(t)}. \qquad (8)$$

For straight-line trajectories, $R(t)$ takes the form

$$R(t) = \sqrt{(x - b)^2 + (y - (y_0 + vt))^2 + z^2}, \qquad (9)$$

with the initial wave functions of the neutral targets

$$P(x, y, z, t = 0) = P_{1s}(x, y, z) \qquad (10)$$

where $P_{1s}(x, y, z)$ is the ground state of the moving H or He atom. The asymptotic wave function, $P(x, y, z, t \to \infty)$, is obtained by propagating the time-dependent Schrödinger equation until the projectile has moved well beyond the target. A time step of 0.02 (atomic units) was used. The probability for CX at impact parameter b then follows as

$$C_{n\ell m}(v, b) = \int_{-\infty}^{\infty} dx \int_{-\infty}^{\infty} dy \int_{0}^{\infty} dz \times |P_{n\ell m}^*(x, y, z)P(x, y, z, t \to \infty)|^2 \qquad (11)$$

---

where $P_{n\ell m}(x, y, z)$ and $P^*_{n\ell m}(x, y, z)$ are the ground and excited states of the stationary Ne^{10+} ion. Finally, the $n\ell$-resolved cross section for a specific velocity v is calculated as

$$\sigma_{n\ell} = 2\pi \sum_m \int_0^\infty C_{n\ell m}(v, b)b\,db. \quad (12)$$

For both targets (H, He), the TDL calculations were carried out at collision energies of 1, 2, 3, 4, and 5 keV amu^{-1}, each at 70 impact parameters (in atomic units) between 0.1 and 20. The (x, y, z) lattice encompassed $720 \times 720 \times 360$ points with a uniform grid spacing of $\delta x = \delta y = \delta z = 0.10$. The lattice extends from -36.0 to $+36.0$ in the x and y directions and from 0.0 to $+36.0$ in the z direction. Each of the 350 TDL calculations for the H and He atoms were carried out on the (x, y, z) lattice spread out over $24 \times 24 \times 12$ cores on parallel computers. Reflections at the boundaries are suppressed by exponential masking (Pindzola & Schultz 2008). Cross sections for the $Ne^{10+} + H$ and $Ne^{10+} + He$ systems calculated in this manner are tabulated in Tables 1 and 2.

2.2. Energy Levels and Transition Rates

To calculate energy levels and transition rates for H-like Ne following CX, we employed the Flexible Atomic Code (FAC; Gu 2008). We considered all configurations up to $n = 9$ with $l_{max} = 8$, where both the Breit interaction and electron self-energy were included. All levels of similar parity were allowed to mix. Our calculated level energies agree with those in the NIST Atomic Spectra Database (ASD; Kramida et al. 2020) at the $\sim$meV level. We compared our transition rates to the ab initio calculation by Popov & Maiorova (2017) and the data in the AtomDB database (Foster & Heuer 2020).[2] Transition rates for both allowed and forbidden transitions are in excellent agreement at the $\ll 1\%$ level.

Atomic data generated by FAC is j-resolved and reported in jj-coupling notation. Using the $jj2lsj$ code (Gaigalas et al. 2017), the wave function expansions were transformed from jj to LSJ coupling, and the levels in our structure calculation were found to be of high purity. To match the structural resolution of the TDL cross sections, FAC levels and transition rates were then transformed from LSJ-resolved to LS-resolved by the following procedure. The LS multiplet energies E_{LS} are calculated as

$$E_{LS} = \frac{\sum_J (2J + 1)E_{LSJ}}{\sum_J (2J + 1)} \quad (13)$$

where the contribution of each LSJ level to the LS-resolved multiplet is weighted by its degeneracy, $2J + 1$. For each pair of multiplets, U and L, the energy of the transition $U \rightarrow L$ follows from the difference of the upper and lower multiplet energies. The transition rate from multiplet U to L, $A_{U\rightarrow L}$, is calculated as

$$A_{U\rightarrow L} = \frac{\sum_l \sum_u (2u + 1)A_{u\rightarrow l}}{\sum_u (2u + 1)} \quad (14)$$

where the transition rate of each j-resolved upper multiplet level is weighted by its statistical weight, and the sums are carried out over the LSJ-resolved levels u and l of the upper and lower multiplets, respectively.

---

[2] Also available at http://www.atomdb.org/Webguide/webguide.php.

Table 1
Time-dependent Lattice $n\ell$-resolved Charge Exchange Cross Sections for $Ne^{10+} + H$

n	ℓ	Energy 1	2	3	4	5
1	0	2.24E-29	1.34E-29	1.53E-29	1.65E-29	2.52E-29
2	0	1.23E-25	1.06E-25	1.58E-26	1.44E-26	1.54E-25
2	1	1.41E-24	7.31E-25	1.29E-25	1.24E-26	5.81E-26
3	0	1.18E-22	1.09E-22	1.06E-22	3.59E-22	1.54E-21
3	1	5.21E-23	7.42E-23	1.45E-22	2.16E-22	7.63E-22
3	2	5.21E-24	2.11E-23	1.13E-22	2.61E-22	1.54E-21
4	0	8.19E-20	3.22E-19	3.36E-19	1.02E-18	1.59E-18
4	1	4.02E-20	1.39E-19	5.13E-19	1.40E-18	3.45E-18
4	2	1.02E-20	2.12E-19	1.25E-18	2.53E-18	3.66E-18
4	3	1.46E-20	1.68E-19	7.66E-19	1.40E-18	2.20E-18
5	0	2.95E-16	2.15E-16	7.95E-17	4.90E-17	3.89E-17
5	1	3.16E-17	1.92E-16	3.27E-16	3.37E-16	2.86E-16
5	2	4.00E-17	9.52E-17	1.52E-16	1.83E-16	2.03E-16
5	3	3.06E-17	7.85E-17	1.06E-16	1.69E-16	2.19E-16
5	4	2.30E-17	5.49E-17	7.17E-17	1.02E-16	1.53E-16
6	0	1.92E-16	8.56E-17	4.96E-17	4.26E-17	3.73E-17
6	1	1.40E-15	9.41E-16	8.15E-16	6.32E-16	4.89E-16
6	2	7.78E-16	8.92E-16	8.53E-16	7.59E-16	6.81E-16
6	3	1.02E-15	1.19E-15	1.20E-15	1.14E-15	1.08E-15
6	4	1.10E-15	1.25E-15	1.32E-15	1.41E-15	1.40E-15
6	5	1.11E-15	1.15E-15	9.96E-16	1.10E-15	1.28E-15
7	0	5.97E-18	5.48E-18	4.29E-18	6.08E-18	7.00E-18
7	1	3.88E-16	1.88E-16	1.40E-16	1.03E-16	8.75E-17
7	2	2.90E-16	1.89E-16	1.68E-16	1.39E-16	1.37E-16
7	3	3.80E-16	2.84E-16	2.67E-16	2.48E-16	2.55E-16
7	4	5.25E-16	4.34E-16	4.78E-16	4.53E-16	4.36E-16
7	5	5.34E-16	6.84E-16	7.28E-16	7.37E-16	6.87E-16
7	6	4.44E-16	6.89E-16	6.29E-16	8.20E-16	9.60E-16
8	0	9.28E-19	1.16E-18	7.30E-19	5.99E-19	7.54E-19
8	1	1.36E-17	6.38E-18	8.16E-18	4.58E-18	4.77E-18
8	2	1.15E-17	8.13E-18	1.00E-17	6.24E-18	9.02E-18
8	3	1.10E-17	1.29E-17	1.61E-17	1.08E-17	1.35E-17
8	4	1.96E-17	2.06E-17	2.91E-17	1.94E-17	2.05E-17
8	5	3.25E-17	2.58E-17	6.18E-17	3.11E-17	2.83E-17
8	6	3.37E-17	4.98E-17	8.60E-17	6.01E-17	4.29E-17
8	7	1.60E-17	5.10E-17	6.20E-17	1.09E-16	1.29E-16
9	0	5.20E-19	3.95E-19	4.22E-19	2.25E-19	2.23E-19
9	1	1.23E-18	1.86E-18	1.65E-18	1.18E-18	9.60E-19
9	2	1.41E-18	2.38E-18	2.13E-18	1.38E-18	1.75E-18
9	3	1.56E-18	2.68E-18	3.28E-18	2.44E-18	2.28E-18
9	4	1.73E-18	3.97E-18	5.65E-18	3.62E-18	4.19E-18
9	5	2.26E-18	5.86E-18	8.87E-18	6.98E-18	6.71E-18
9	6	3.18E-18	4.59E-18	5.81E-18	7.02E-18	9.18E-18
9	7	2.66E-18	3.08E-18	5.36E-18	7.63E-18	1.00E-17
9	8	3.43E-18	4.24E-18	4.88E-18	5.52E-18	7.63E-18

Note. Cross sections are reported in units of cm^2 and energies are reported in keV amu^{-1}.

2.3. X-Ray Cascade Model

The energy levels, transition rates, and $n\ell$-resolved cross sections were incorporated into an X-ray cascade model constructed in Python, with all mathematical operations carried out using NumPy (Harris et al. 2020). We have assumed single-collision and optically thin conditions; a full discussion of this computational approach is available in Rigazio et al. (2002).

Table 2
Time-dependent Lattice $n\ell$-resolved Charge Exchange Cross Sections for
Ne^{10+} + He

n	ℓ	Energy				
		1	2	3	4	5
1	0	2.51E-29	2.73E-29	1.12E-28	5.00E-28	5.20E-28
2	0	4.41E-24	2.20E-24	1.28E-24	6.94E-24	1.05E-23
2	1	5.95E-23	1.17E-23	1.27E-24	3.98E-25	2.26E-24
3	0	3.27E-20	2.09E-19	5.07E-19	1.22E-18	1.39E-18
3	1	1.61E-21	2.72E-20	1.33E-19	4.27E-19	7.92E-19
3	2	4.54E-21	4.50E-20	2.38E-19	6.62E-19	1.70E-18
4	0	4.47E-16	2.84E-16	1.83E-16	1.30E-16	9.98E-17
4	1	5.65E-17	2.06E-16	3.11E-16	3.94E-16	4.56E-16
4	2	6.96E-17	1.51E-16	1.62E-16	1.69E-16	1.86E-16
4	3	4.60E-17	8.81E-17	1.20E-16	1.32E-16	1.50E-16
5	0	5.50E-17	3.30E-17	2.12E-17	1.69E-17	1.61E-17
5	1	9.43E-17	6.54E-16	4.62E-16	3.57E-16	2.92E-16
5	2	3.99E-16	3.97E-16	3.66E-16	3.47E-16	3.28E-16
5	3	4.50E-16	5.09E-16	5.84E-16	5.04E-16	4.85E-16
5	4	6.00E-16	5.03E-16	5.10E-16	5.41E-16	4.99E-16
6	0	4.94E-19	3.29E-19	3.19E-19	7.56E-19	1.10E-18
6	1	2.39E-17	1.50E-17	1.17E-17	6.36E-18	7.63E-18
6	2	2.91E-17	1.21E-17	5.68E-18	9.57E-18	1.15E-17
6	3	3.91E-17	2.52E-17	1.48E-17	9.37E-18	2.29E-17
6	4	2.73E-17	3.66E-17	4.11E-17	2.55E-17	3.00E-17
6	5	1.34E-17	2.01E-17	3.25E-17	4.80E-17	4.81E-17
7	0	1.48E-20	1.17E-19	1.41E-19	1.48E-19	1.64E-19
7	1	5.09E-19	5.66E-19	1.86E-18	1.35E-18	1.20E-18
7	2	4.46E-19	6.59E-19	1.55E-18	1.34E-18	1.36E-18
7	3	3.29E-19	9.37E-19	1.85E-18	2.67E-18	1.78E-18
7	4	4.39E-19	8.92E-19	1.40E-18	4.43E-18	5.07E-18
7	5	4.57E-19	6.51E-19	1.09E-18	1.51E-18	5.58E-18
7	6	3.23E-19	4.72E-19	8.96E-19	1.19E-18	1.23E-18
8	0	2.03E-19	1.72E-19	9.39E-20	1.27E-19	1.00E-19
8	1	3.24E-19	6.14E-19	4.88E-19	7.23E-19	5.44E-19
8	2	4.38E-19	5.87E-19	6.28E-19	6.16E-19	5.83E-19
8	3	5.09E-19	7.29E-19	7.40E-19	9.25E-19	5.62E-19
8	4	3.96E-19	7.14E-19	5.73E-19	6.90E-19	8.81E-19
8	5	4.01E-19	4.48E-19	5.17E-19	6.93E-19	7.95E-19
8	6	5.11E-19	4.49E-19	6.18E-19	7.08E-19	9.23E-19
8	7	4.67E-19	5.31E-19	6.34E-19	6.59E-19	6.76E-19
9	0	4.53E-19	1.31E-19	6.86E-20	9.11E-20	9.99E-20
9	1	1.11E-18	4.98E-19	2.62E-19	2.45E-19	2.25E-19
9	2	1.17E-18	6.40E-19	5.16E-19	6.07E-19	5.74E-19
9	3	1.54E-18	7.75E-19	6.65E-19	8.18E-19	9.07E-19
9	4	1.31E-18	9.84E-19	1.03E-18	1.36E-18	1.77E-18
9	5	1.17E-18	1.11E-18	1.51E-18	1.95E-18	2.35E-18
9	6	1.68E-18	1.51E-18	1.73E-18	2.38E-18	2.98E-18
9	7	2.10E-18	1.97E-18	2.32E-18	2.40E-18	2.63E-18
9	8	4.38E-18	2.92E-18	2.07E-18	1.63E-18	1.62E-18

Note. Cross sections are reported in units of cm^2 and energies are reported in keV amu^{-1}.

Synthetic X-ray spectra are generated by computing the radiative cascade of each possible capture channel. Each cascade calculation starts with an initially occupied energy level, denoted $N_{n'\ell'}$ with unit population, and population is transferred to each lower level $N_{n\ell}$ according to

$$N_{n\ell} = N_{n'\ell'} \times \frac{A_{n'\ell' \to n\ell}}{\alpha} \qquad (15)$$

where α is the sum of the transition rates out of level $N_{n'\ell'}$, $A_{n'l' \to nl}$ is the transition rate from level $(n'l')$ to level (nl), and $N_{n'\ell'}$ is the population of the upper level of the transition. The
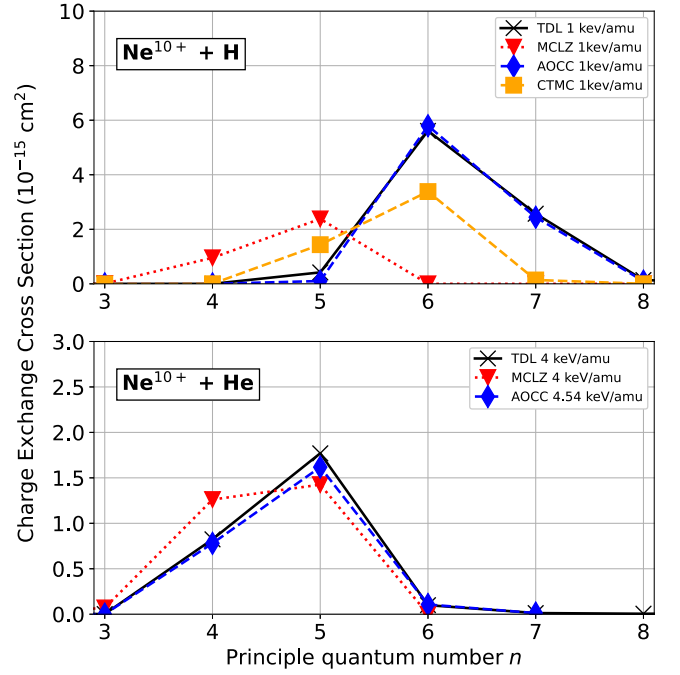

Figure 1. (Top) n-resolved CX cross sections for Ne^{10+}+ H at 1 keV amu^{-1} calculated with the following methods: TDL (present work, black ×) vs. MCLZ cross sections (red ▽, Mullen et al. 2016), atomic orbital close coupling (AOCC, blue ◊, Cumbee et al. 2016), and classical-trajectory Monte Carlo (CTMC, orange □, Cumbee et al. 2016). (Bottom) n-resolved CX cross sections for Ne^{10+}+ He at 4 keV amu^{-1} for TDL (present work, black ×), MCLZ (red ▽, Mullen et al. 2016), and AOCC (blue ◊, 4.54 keV amu^{-1}, Liu et al. 2014).

intensity of the transition out of level $N_{n'\ell'}$ to level $N_{n\ell}$, in units of photons per second, is thus

$$I_{n'\ell' \to n\ell} = N_{n'\ell'} \times \frac{A_{n'\ell' \to n\ell}}{\alpha}. \qquad (16)$$

Iteration over the energy levels in decreasing energy order and transferring population to all possible lower levels in accordance with the branching ratios of the upper levels yields the (relative) line intensity of each possible transition for a given initial capture channel. The "final" X-ray spectrum is constructed as the sum of all possible cascades, with each cascade weighted by the CX cross section of the initial capture channel.

In our spectral models, we considered up to $n = 9$ and $\ell = 8$ levels with all electric-dipole (E1) and magnetic-dipole (M1) transitions included in the model. To validate our computational method, we compared our cascade model against the implementation available in the KRONOS code suite (Mullen et al. 2016; Cumbee et al. 2016; Lyons et al. 2017). Lyman and Balmer line ratios for CX between bare Ne/Mg incident on atomic H/He, generated from MCLZ data in the KRONOS database, from both codes show differences at the ≪1% level. Similar agreements are found between the present work and the collisional-radiative model built into the FAC.

3. Results

3.1. Cross Sections and Momentum Distributions

Figure 1 shows the total n-resolved CX cross sections for the considered collision systems from TDL (present work, produced via summation over ℓ), MCLZ (KRONOS), and AOCC/CTMC data from Cumbee et al. (2016) as a function of principal quantum
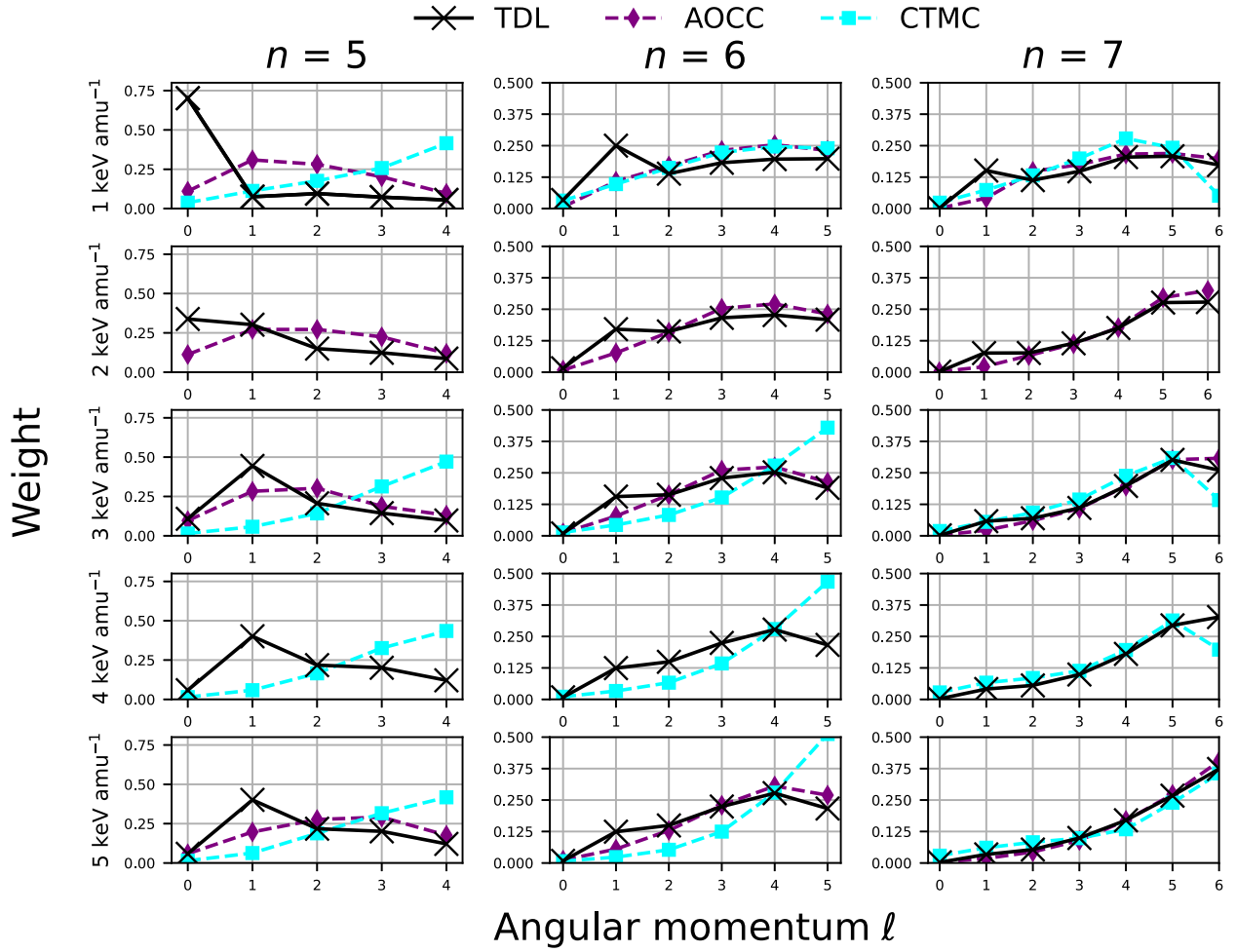
Figure 2. Comparison of the ℓ distribution of post-CX capture states for Ne^{10+} and atomic hydrogen. TDL ℓ distributions (present, black $\times$) for $n = 5$–7 are compared to AOCC ($\Diamond$) and CTMC ($\Box$) data sourced from the KRONOS database (Lyons et al. 2017; Cumbee et al. 2016). All weights are normalized such that $\sum W = 1$ for each n shell.

number at select collision energies. For the atomic hydrogen target the TDL, CTMC, and AOCC methods all predict the dominant capture channel as $n = 6$ at all available energies. The MCLZ data predicts little to no capture in $n = 6$ and favors $n = 5$ as the dominant capture channel. These trends occur at every collision energy considered (1, 2, 3, 4, and 5 keV amu^{-1}).

For the atomic He target, the TDL (n-resolved) cross sections are similar to those calculated with the MCLZ method at all collision energies with the dominant capture channel as $n = 5$. $n\ell$-resolved AOCC cross sections for the He target were only available at one collision energy, 4.54 keV amu^{-1} (Liu et al. 2014), and the cross sections show good agreement with our TDL data at 4 keV amu^{-1}. Agreement cannot be inferred at other collision energies.

From the $n\ell$-resolved cross sections, the weight of each ℓ channel within a given n shell is computed as

$$W^{\mathrm{TDL}}(n\ell) = \frac{\sigma_{n\ell}}{\sum_{\ell} \sigma_{n\ell}} \qquad (17)$$

where $\sigma_{n\ell}$ is the $n\ell$-resolved cross section (Tables 1 and 2) and the denominator is summed over ℓ for a given n shell. Figure 2 shows the ℓ distributions for the three most important n shells for the Ne^{10+} + H system as a function of collision energy for TDL (black; present), and AOCC/CTMC data from Cumbee et al. (2016). For most channels and energies, the similarity

between AOCC and TDL data is not unexpected. Both methods solve the time-dependent Schrödinger equation. The TDL data, however, show a marked increase in $\ell = 0$ capture for $n = 5$ at low energies and a gradual shift from favoring $\ell = 0$ to $\ell = 1$ with increasing collision energy. For $n = 6, 7$ the TDL data show enhanced population (with respect to equivalent AOCC data) in $\ell = 1$ for most energies.

CTMC data for bare ions colliding with atomic hydrogen at 50 and 100 keV amu^{-1} by Olson (1981) revealed two trends in the ℓ distributions of capture states. For $n > n_{\max}$, the ℓ distribution peaks around $\ell \sim n$. For $n < n_{\max}$, capture is favored for larger values of ℓ. We note that the relevant collision energies here, 1–5 keV amu^{-1}, are a factor of 10–20 lower than those explored in Olson (1981). The CTMC data of Cumbee et al. (2016) at 1–5 keV amu^{-1} show quasi-statistical behavior for $n = 5$. For $n = 6$, the population of the higher ℓ states increases with energy. The $n = 7$ channel shows a peaked behavior which disappears between 4 and 5 keV amu^{-1} and transforms into a greater-than-statistical distribution at 5 keV amu^{-1}. These trends in the higher n shells are opposite to those found at the much higher energies in Olson (1981).

Figure 3 shows the TDL ℓ distribution compared to the four analytic ℓ distributions for the Ne^{10+} + H system for the most important capture channels, $n = 5$–7. The TDL ℓ distribution of the $n = 5$ capture channel is most similar to a low-energy
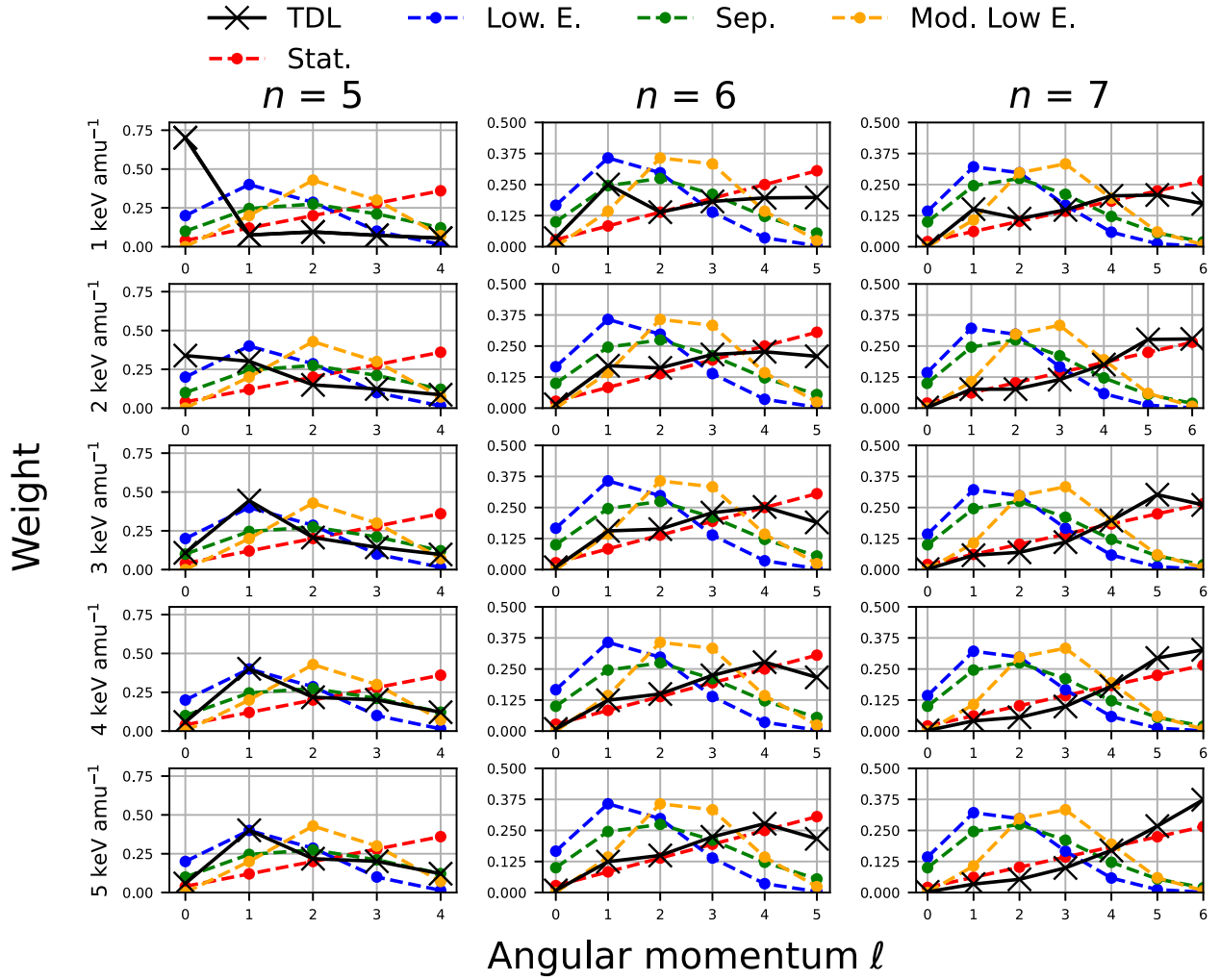
Figure 3. Comparison of the ℓ distribution of post-CX capture states for Ne^{10+} and atomic hydrogen. TDL ℓ distributions (present, black ×) for $n = 5$–7 are compared to the four analytical ℓ distributions (colored °). All weights are normalized such that $\sum W = 1$ for each n shell.

distribution, though capture into $n = 5$ is substantially smaller than $n = 6$ (see Figure 1) and has a minor effect on the resulting X-ray spectra. For $n = 6$–7, the ℓ distribution is close to a statistical distribution. The capture into the $\ell = 6$ channel in $n = 7$ shifts from substatistical to greater-than-statistical between 1 and 5 keV amu^{-1}, the latter being opposite to the trend identified by Olson (1981) at higher energies.

Figure 4 shows similar comparisons for the Ne^{10+}+He system for $n = 4$–6. AOCC data from Liu et al. (2014) at 4.54 keV amu^{-1} are shown alongside the present TDL data. The TDL data show similarities to the AOCC data, including an enhancement of the highest ℓ state in $n = 6$. Both the H and He TDL data also show an enhancement of $\ell = 0$ states for the n shell immediately below the dominant capture channel. The source of this enhancement is common to both H and He targets, and could result from the choice of straight-line instead of Coulombic trajectories, though the exact cause is unknown at this time. This enhancement decreases with increasing collision energy (Figure 2) and disappears for the dominant n shells by ∼3 keV amu^{-1}. In He, the data may also be affected by the treatment of He as a one-electron system in the presence of a model potential (Equation (8)), i.e., the lack of explicit treatment of He as a two-electron system. AOCC calculations of highly charged ion–He collision systems in which He is explicitly treated as a two-electron system are discussed at

length in Fritsch & Lin (1991) and showed agreement with experimental measurements at energies above ∼10 keV amu^{-1}. The present comparisons between TDL data at 4 keV amu^{-1} and AOCC data at 4.5 keV amu^{-1} suggest a one-electron treatment for He targets may be valid to even lower collision energies.

In both targets, the TDL data also exhibit two unique behaviors. For $n \geqslant n_{\text{dominant}}$ where n_{dominant} has the largest n-resolved cross section, the TDL ℓ distribution is most similar, but not equivalent to, a statistical distribution. For $n < n_{\text{dominant}}$, the ℓ distribution tends toward a low-energy distribution with increasing energy. These two unique trends are opposite to those observed in the CTMC calculations at 50 and 100 keV amu^{-1} by Olson (1981).

3.2. Diagnostic Line Ratios

Due to differing n-resolved cross sections, unnormalized intensities of all features can show differences as large as 20%–40%. A discussion of differing cross sections and their impact on spectral models is beyond the scope of this work, though a lengthy discussion is available in Gu et al. (2022). We note that the $\Delta n = 0, 1, 2, \ldots$ transitions in our models with H and He targets yield a forest of lines beneath 200 eV, many of which vary strongly with collision energy. The energies of these
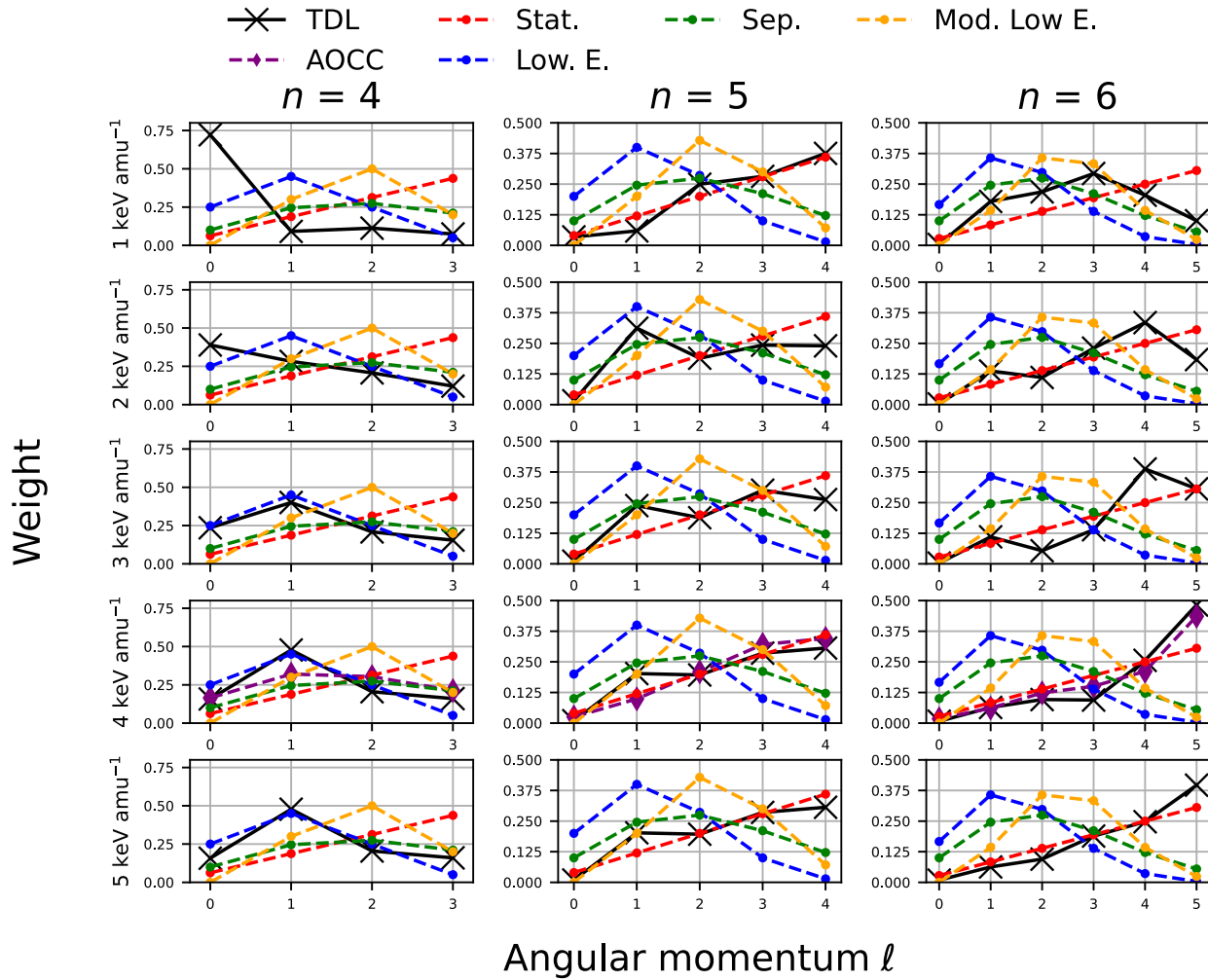
Figure 4. Comparison of the ℓ distribution of post-CX capture states for Ne^{10+} and atomic helium. TDL ℓ distributions (present, black ×) for $n = 4$–6 are compared to the four analytical ℓ distributions: statistical (red, Equation (3)), low energy (blue, Equation (2)), separable (green, Equation (4)), and modified low energy (orange, Equation (5)). AOCC data from Liu et al. (2014) at 4.54 keV amu^{-1} (purple) are plotted alongside the 4 keV amu^{-1} data. All weights are normalized such that $\sum W = 1$ for each n shell.

transitions are outside the bandpass of upcoming X-ray observatories, and no currently flown observatories are equipped to capitalize on these diagnostic lines. However, these lines may prove to be useful in the laboratory to advance an understanding of both SEC and MEC processes. For He-like ions produced by either SEC with H-like ions or double-electron capture with bare ions, both the X-ray and EUV spectra may be not only desired but necessary to understand the capture and subsequent emission features (Suraud et al. 1991; Bodewits & Hoekstra 2019).

X-ray emission of H-like ions resulting from CX depends on both the principal quantum numbers n into which the electron is captured, as well as the angular momentum ℓ. We first investigated the effect of differing n-resolved cross sections on synthetic X-ray spectra in each collision system. The strongest Lyman and Balmer lines, for a given collision energy and ℓ distribution, show very minor differences that can be attributed to different n-resolved cross sections. For $\Delta n = 0$, 1 cascades between 0 and 200 eV photon energy, differences are more pronounced.

From our models, we extracted line ratios for the strongest lines of the Lyman and Balmer series as a function of collision energy. Figure 5 shows the five strongest line ratios (with

respect to Lyα) in each of the Lyman and Balmer series as a function of collision energy for Ne^{10+} + H. Most Lyman line ratios, relative to Lyα, for TDL, AOCC, CTMC, and MCLZ + statistical-ℓ models are generally in agreement. For the Balmer series, the TDL, AOCC, and MCLZ + statistical-ℓ line ratios are in agreement. We note that both Ly-ζ and Ba-ϵ are driven by capture into $n = 7$, for which the TDL ℓ distribution can vary strongly with collision energy. If observed, these two lines offer a potential diagnostic of the collision energy.

Figure 6 shows Lyman and Balmer line ratios extracted from our spectral models of the Ne^{10+} + He system as a function of collision energy. Compared to the hydrogen target, agreement for the He case between $n\ell$-resolved and n-resolved (ℓ applied) models is less certain. For the Lyman series, agreement between TDL and ℓ-applied models shifts from statistical-ℓ at 1 keV amu^{-1} to separable/modified low-energy ℓ models at the higher energies.

Spectral measurements of Ne^{10+} + He collisions at 4.5 keV amu^{-1} by Ali et al. (2010), gated for SEC events, provide a test of these data and the treatment of He as a one-electron system. Figure 7 shows a comparison of the experimental spectra of Ali et al. (2010) to all available n-resolved (ℓ applied) and $n\ell$-resolved spectral models. Two peaks are visible, Lyα
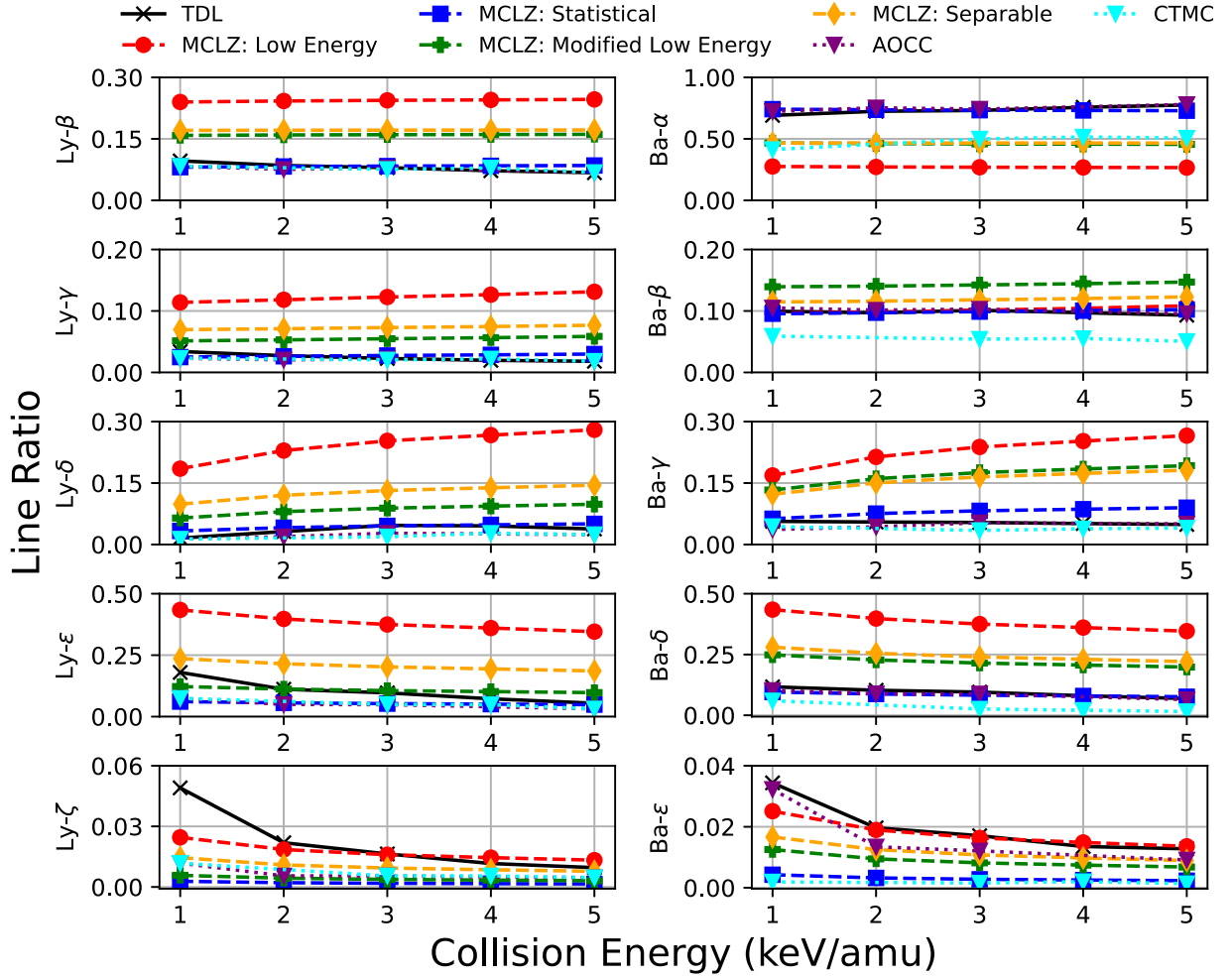
Figure 5. Lyman (left) and Balmer (right) line ratios with respect to Lyα for Ne^{10+} + H charge exchange as a function of collision energy, calculated with different methods. Line ratios were constructed from the X-ray cascade model (Section 2.3). $n\ell$-resolved cross sections were used for TDL (present work; black ×). n-resolved MCLZ data (Lyons et al. 2017) was used to generate the line ratios for each choice of analytical ℓ distribution. Where available, line ratios from $n\ell$-resolved data computed with the AOCC and CTMC methods are shown (Cumbee et al. 2016).

(1022 eV) and the blend of Lyβ, Lyγ, ..., labeled as Lyβ+. The TDL data lies intermediate of the two extremes of the MCLZ with analytic ℓ distributions, but underestimates the strength of Lyβ by a factor of ∼3. Multiplication of the Lyβ intensity by a factor of 3 (red dashed curve) brings the modeled spectra into agreement with the majority of the experimental measurements of Ali et al. (2010). Test calculations manually adjusting the ℓ distribution of the $n = 4, 5$ channels shows that the TDL spectra are relatively insensitive to changes in the $n = 4$ cross sections, and are largely dependent on the ℓ distribution of the $n = 5$ capture states. We find that the low-energy ℓ distribution greatly overestimates the strength of the Lyman series above $n = 2$, and both the AOCC (purple) and MCLZ + statistical-ℓ (red) underestimate the strength of the Lyβ+ feature. The separable and modified low-energy ℓ distributions yield the closest agreement with experiments, though both underpredict the intensity of all components of the Lyβ+ feature.

The careful reader will notice that the MCLZ curves shown here differ from those of Cumbee et al. (2016). The cross sections used in Cumbee et al. (2016) were updated by the computed data now available in the KRONOS database (R. Cumbee; private communication), and the cross sections in KRONOS are of an expected higher quality compared to those used in the earlier analysis of Cumbee et al. (2016).

An additional test of these data is the hardness ratio, defined as

$$H = \sum_{n>2} \frac{I(n \to 1)}{I(2 \to 1)} \qquad (18)$$

where $I(n \to 1)$ is the intensity of each Lyman series line from $n > 2$ and $I(2 \to 1)$ is the intensity of Lyα in photons per second. The hardness ratios extracted from n- and $n\ell$-resolved spectral models are shown in Figure 8. For a hydrogen target, both AOCC and TDL data produce similar hardness ratios above 1 keV amu^{-1}. The agreement between $n\ell$-resolved model hardness ratios and the MCLZ + statistical-ℓ hardness ratio is immediately apparent and results from the similarities in both n-resolved cross sections (Figure 1) and ℓ distributions (Figures 2 and 3). Despite large differences in individual line ratios, the hardness ratio from CTMC data is comparable to that extracted from TDL and AOCC data. For He targets, the MCLZ + separable ℓ, MCLZ + modified low-energy ℓ, and TDL data show a similar hardness ratio, consistent with the agreement found in comparison to experimental spectra (Figure 7).
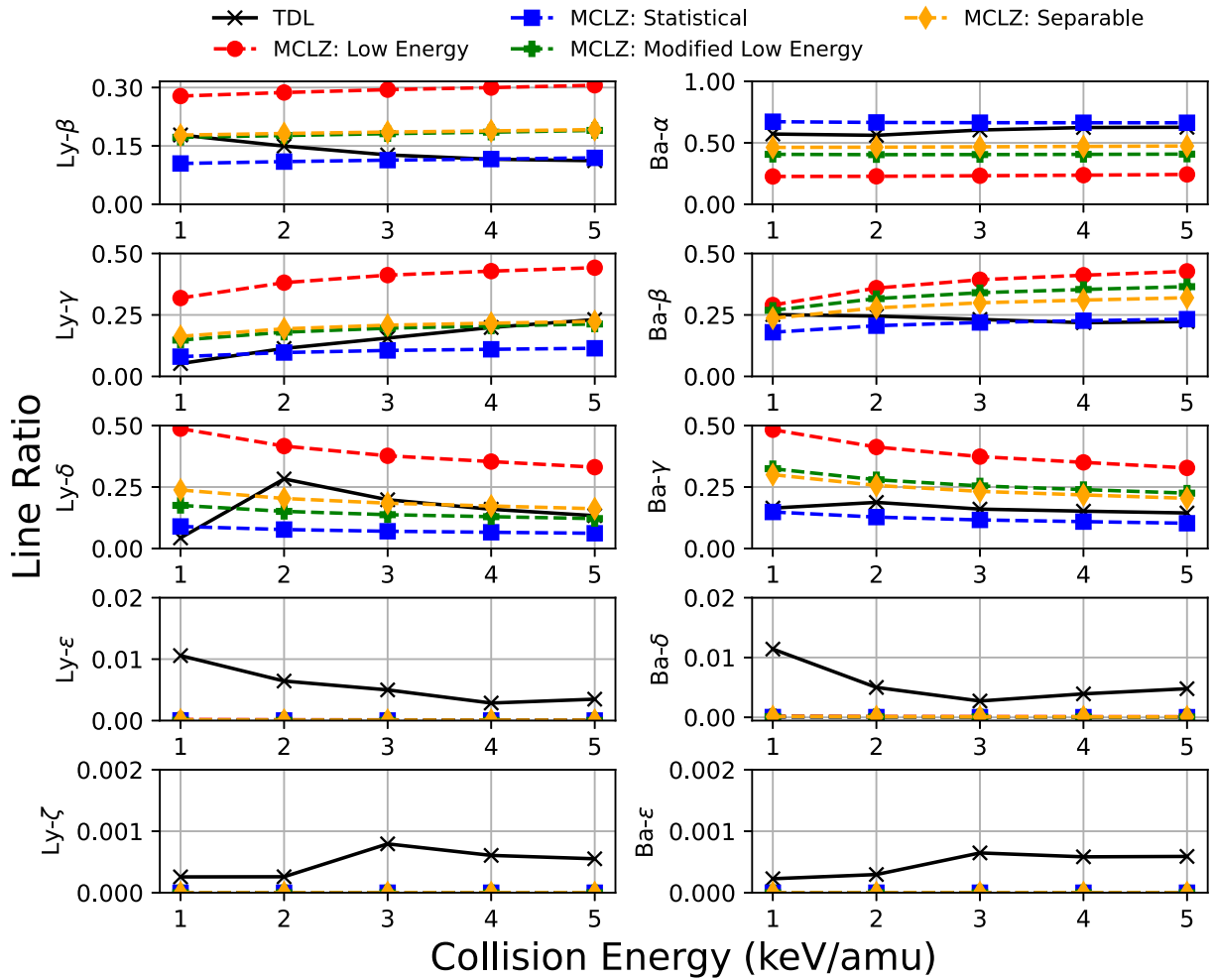
Figure 6. Lyman (left) and Balmer (right) line ratios with respect to Lyα for Ne^{10+} + He charge exchange as a function of collision energy, calculated with different methods. Line ratios were constructed from the X-ray cascade model (Section 2.3). $n\ell$-resolved cross sections were used for TDL (present work; black ×). n-resolved MCLZ data (Lyons et al. 2017) was used to generate the line ratios for each choice of analytical ℓ distribution.

4. Discussion

Present spectrometers in orbit such as the Chandra Advanced CCD Imaging Spectrometer (ACIS) with spectral resolution of order ~50–100 eV cannot fully resolve the Lyman series emitted by many CX-produced H-like ions. For low signal-to-noise spectra of, e.g., comets, only a handful of Gaussian distributions may be utilized to model the most important CX features (see Ewing et al. 2013; Lisse et al. 2013; Bonamente et al. 2021), and will depend on the observed features and the state of the solar wind (Bonamente et al. 2021). More complicated models are often constructed by fixing the relative contribution of each ion's spectrum (Bodewits et al. 2007; Carter et al. 2010; Snios et al. 2016). In such cases the differences introduced by analytic ℓ distributions of capture states may be difficult to discern.

At high spectral resolution, the accuracy of atomic parameters that determine the strengths of individual features becomes increasingly important. In its short lifespan, the high-resolution spectra provided by Hitomi led to unprecedented science (Aharonian et al. 2016, 2017). These spectra revealed many features which were blended or undetectable in lower-resolution spectra, and later prompted scrutiny of the atomic data utilized in X-ray models (see, e.g., Aharonian et al. 2018). It is expected that high-resolution spectra from XRISM will

again prompt a reexamination of the atomic data used in widely distributed X-ray modeling codes. In many ways this has already begun, as evidenced by the two White Papers describing similar efforts (Kallman et al. 2019; Smith et al. 2019). Explaining CX emission features alone will require a detailed understanding of both SEC and MEC for a wide range of collision partners and collision energies.

In broad terms, there is consensus on the n-dependent CX cross sections for the bare-ion collision systems presented in this article. For an atomic H target, the TDL ℓ distributions are similar to the low-energy distribution for $n < n_{\text{dominant}}$, and the statistical distribution for $n \geqslant n_{\text{dominant}}$. We reiterate that these trends are opposite to those derived from CTMC calculations at higher collision energies by Olson (1981).

For atomic H targets, the statistical ℓ distribution appears to yield line ratios similar to those produced from $n\ell$-resolved methods. For the He target, no consensus was found between the limited $n\ell$-resolved data and n-resolved (ℓ-applied) data, and the scatter in line ratios is considerable. The AOCC hardness ratio at 4.5 keV amu^{-1} is consistent with that of MCLZ+ statistical ℓ models. Both the MCLZ+ separable and MCLZ+ modified low-energy distribution ℓ models, however, lead to Lyβ+ emission (Figure 7) that is more consistent with experimental measurements compared to either AOCC or TDL data. These disagreements between n- and $n\ell$-resolved models
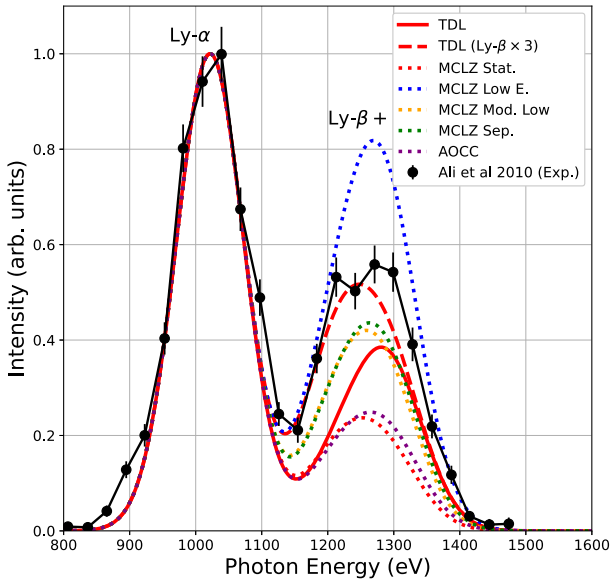
Figure 7. Comparison of experimental single-electron capture spectra of Ne^{10+} + He collisions at 4.5 keV amu^{-1} (black, ~120 eV FWHM resolution) to spectral models. Experimental spectra and error bars (black circles) were digitized from Ali et al. (2010) and Cumbee et al. (2016). Spectral models were convolved with a Gaussian to a resolution of 120 eV FWHM to match the experimental resolution for: TDL cross sections (red solid line), MCLZ + statistical ℓ (red dotted line), MCLZ + low-energy ℓ distribution (blue dotted line), MCLZ + modified low-energy ℓ (orange dotted line), MCLZ + separable ℓ (green line), and AOCC (purple line; Cumbee et al. 2016). A TDL model with the contribution of Lyβ ×3 is shown as a dashed red line (see text).

Figure 8. Hardness ratios extracted from synthetic charge-exchange spectra in the Ne^{10+} + H (top) and Ne^{10+} + He (bottom) collision systems, as a function of collision energy. Hardness ratios (Equation (18)) were calculated from synthetic X-ray spectra for n-resolved MCLZ data with a modified low-energy distribution (▽), statistical (°), low energy (□), and separable (+). TDL hardness ratios are shown for all $n\ell$-resolved cross sections up to $n = 9$ and $l = 8$ (×), $n \leqslant 6/7$ for AOCC (▽), and CTMC (□).

for the He target are not unexpected. The low-energy and statistical ℓ distributions derived by Janev et al. (1983) were derived by assuming an atomic H target.

Characterizing CX between the most abundant ions and astrophysically relevant neutrals (H$_2$, H$_2$O, CO, CO$_2$, He, O$_2$, ...) will require a substantial effort, and the applicability of simple one-electron treatments or the use of straight-line trajectories for these systems is not known. Disagreements between theory and experiment for the simple two-electron collision system, Ne^{10+} + He, motivates additional work in this area. Spectral measurements of these collision systems at solar wind velocities with microcalorimeters (spectral resolution <10 eV) would be capable of measuring both individual Lyman ratios and the hardness ratio as a function of collision energy. Alternatively, the ℓ distribution of capture states could be extracted directly from high-resolution spectra using the methods developed and described by Betancourt-Martinez et al. (2020), and would provide an invaluable benchmark of analytic ℓ distributions.

MEC introduces an additional complexity to atomic data needs. Spectral models with MEC require both radiative and autoionizing capture (Liang et al. 2021), though cross sections for these competing channels are few in number. It is expected that double-electron capture is a significant contributor (Ali et al. 2016; Fogle et al. 2014; Bodewits et al. 2007), and in some cases states as highly excited as $4\ell6\ell'$ may be populated (Flechard et al. 1997). Autoionizing double-electron capture, on the other hand, tends to populate lower n shells after autoionization, resulting in enhanced emission of e.g., Lyα and Lyβ (Seely et al. 2017; Bodewits & Hoekstra 2019).

For collisions with targets having only two electrons, e.g., O^{6+} + He/H$_2$ (Machacek et al. 2014), the contribution of MEC can be

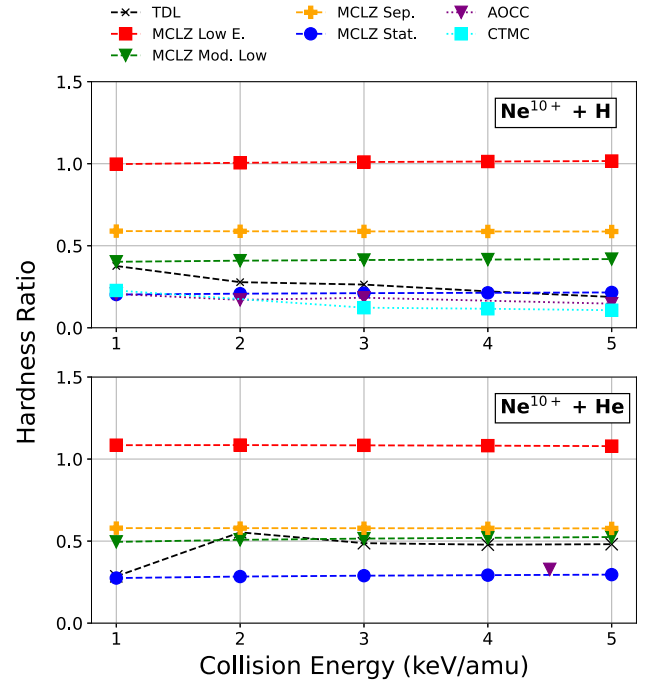low, of order ~10%. For more complicated targets such as H$_2$O, MEC (double, triple, ...) can comprise a larger portion of the total CX cross section of order 20% or more (Machacek et al. 2015). These findings are consistent with other experiments by Ali et al. (2005), who investigated SEC/MEC of 4.5 keV amu^{-1} bare Ne incident on He, Ne, and Ar. For the He target (second ionization potential 54.4 eV) the contribution of MEC was low (⩽13%), but the contribution for targets such as Ar (comparable in ionization potential to e.g., H$_2$O) exceeded 50% (Ali et al. 2005). While as many as six electron captures were observed to be initially captured in a single collision with atomic Ar, the majority of the MEC events led to final charge states within 1–2 of the initial ion charge (Ali et al. 2005).

The electronic structures of the collision partners complicate qualitative predictions of MEC. Following an initial MEC, one or more autoionizations can drive the system to stability. Calculation of these autoionizing/radiative cascades can require electronic structure data for hundreds to thousands of configurations. For example, in collisions of Fe$^{(5-13)+}$ impacting on H$_2$O, MEC (double, triple, ...) constituted a large (>20%) portion of the total cross section (Simcic et al. 2010a). As evidenced in their Monte Carlo calculations, the uncertainties in the complex autoionizing and radiative cascades introduced uncertainties in their MEC cross sections as high as 42% on average. For H$_2$O, their Monte Carlo calculations found reasonable agreement within the combined experimental/theoretical uncertainties for single-, double-, and triple-electron capture cross sections for most charge states of Fe. However, the same approach applied to CO and CO$_2$ targets underestimated the cross sections for double and triple capture by factors of 2–3, with some uncertainties as high as 100% (Simcic et al. 2010b). In general, the impact of autoionization on the MEC process appears to grows in magnitude with increasing charge

state (Simcic et al. 2010a, 2010b), but a complete understanding of this process remains an open question.

Both an understanding of and atomic data for multielectron neutrals and capture processes are expected to grow in importance with the availability of high-resolution astrophysical X-ray spectra. The Cold Target Recoil Ion Momentum Spectroscopy (COLTRIMS) technique, as shown by Ali et al. (2005) and Ali et al. (2016), is well suited to characterizing the CX process in the laboratory and providing critical atomic data for X-ray models. Similar experiments utilizing a microcalorimeter and a velocity-tunable crossed-beam apparatus are planned by the present authors for Ne^{10+} + He in the coming months at the Clemson University Electron Beam Ion Trap (CUEBIT) facility. The measured Lyman ratios will provide a direct test of both n- and $n\ell$-resolved cross sections presented here and will probe the validity of a one-electron treatment for He targets and the use of straight-line versus Coulombic trajectories in CX cross section calculations at solar wind energies. Future experiments will extend the method to other neutrals of astrophysical interest.

5. Conclusion

We reported new calculations of $n\ell$-resolved CX cross sections for bare Ne ions incident on atomic H and He using the time-dependent lattice (TDL) method at collision energies of typical solar wind conditions, 1–5 keV amu^{-1}. Using a radiative cascade model, we computed synthetic X-ray spectra from both n- and $n\ell$-resolved CX cross sections and extracted line ratios with respect to Lyα. We investigated the effect of differing n-resolved data on the X-ray spectrum and found minor differences in Lyman and Balmer line ratios, confirming that differences in spectral features are primarily driven by the ℓ distribution.

For the atomic hydrogen target, the ℓ distribution extracted from our $n\ell$-resolved cross sections is most similar to the statistical ℓ distribution (Equation (3)) and agrees well with that extracted from AOCC cross sections (Cumbee et al. 2016). These ℓ distributions follow two unique trends which are opposite to those observed at high collision energies (Olson 1981). At solar wind velocities of 1–5 keV amu^{-1}, the TDL, AOCC, and MCLZ+ statistical ℓ spectral models show good agreement for most line ratios.

For the He target, the agreement between line ratios produced from n- and $n\ell$-resolved data is scattered. Comparisons to measured X-ray spectra of Ne^{10+} collisions with He at 4.5 keV amu^{-1} showed that the available $n\ell$-resolved data either overpredicts the intensity of Lyα, or underpredicts the intensities of Lyβ and other Lyman lines. Both the MCLZ+ separable ℓ and MCLZ+ modified low-energy ℓ spectral models show better agreement with experiment than the available $n\ell$-resolved data. Comparisons of Ne^{10+} + He CX spectral models using both n- and $n\ell$-resolved cross sections showed that the treatment of He as a one-electron system and/ or the use of straight-line trajectories may provide an insufficient description of the CX process at solar wind energies. COLTRIMS measurements, in combination with microcalorimeter-resolution spectra, are planned by the present authors in the near future to test both n- and $n\ell$-resolved data for the Ne^{10+} + He system at solar wind velocities.

ORCID iDs

S. J. Bromley ⓘ https://orcid.org/0000-0003-2110-8152
M. Pindzola ⓘ https://orcid.org/0000-0001-6787-9249
D. Bodewits ⓘ https://orcid.org/0000-0002-2668-7248
M. R. Fogle ⓘ https://orcid.org/0000-0003-3511-262X

References

Aharonian, F., Akamatsu, H., Akimoto, F., et al. 2016, Natur, 535, 117
Aharonian, F., Akamatsu, H., Akimoto, F., et al. 2017, Natur, 551, 478
Aharonian, H., Collaboration, F., Akamatsu, H., Akimoto, F., et al. 2018, PASJ, 70, 12
Ali, R., Beiersdorfer, P., Harris, C. L., & Neill, P. A. 2016, PhRvA, 93, 012711
Ali, R., Neill, P. A., Beiersdorfer, P., et al. 2005, ApJ, 629, L125
Ali, R., Neill, P. A., Beiersdorfer, P., et al. 2010, ApJ, 716, L95
Beiersdorfer, P., Lisse, C. M., Olson, R. E., Brown, G. V., & Chen, H. 2001, ApJ, 549, L147
Betancourt-Martinez, G. L., Cumbee, R. S., & Leutenegger, M. A. 2020, AN, 341, 197
Bodewits, D., Christian, D. J., Torney, M., et al. 2007, A&A, 469, 1183
Bodewits, D., & Hoekstra, R. 2007, PhRvA, 76, 032703
Bodewits, D., & Hoekstra, R. 2019, Atoms, 7, 17
Bonamente, E., Christian, D. J., Xing, Z., et al. 2021, PSJ, 2, 224
Butler, S. E., & Dalgarno, A. 1980, ApJ, 241, 838
Carter, J. A., Sembay, S., & Read, A. M. 2010, MNRAS, 402, 867
Cumbee, R. S., Liu, L., Lyons, D., et al. 2016, MNRAS, 458, 3554
Dennerl, K. 2010, SSRv, 157, 57
Ewing, I., Christian, D. J., Bodewits, D., et al. 2013, ApJ, 763, 66
Flechard, X., Duponchel, S., Adoui, L., et al. 1997, JPhB, 30, 3697
Fogle, M., Wulf, D., Morgan, K., et al. 2014, PhRvA, 89, 042705
Fogle, M. R., & Pindzola, M. S. 2020, JPhB, 53, 095203
Foster, A. R., & Heuer, K. 2020, Atoms, 8, 49
Fritsch, W., & Lin, C. 1991, PhR, 202, 1
Fujimoto, R., Mitsuda, K., Mccammon, D., et al. 2007, PASJ, 59, 133
Gaigalas, G., Fischer, C. F., Rynkun, P., & Jönsson, P. 2017, Atoms, 5, 6
Gu, L., Mao, J., O'Dea, C. P., et al. 2017, A&A, 601, A45
Gu, L., Shah, C., & Zhang, R. 2022, Senso, 22, 752
Gu, M. F. 2008, CaJPh, 86, 675
Harris, C. R., Millman, K. J., van der Walt, S. J., et al. 2020, Natur, 585, 357
Jain, A., Lin, C. D., & Fritsch, W. 1987, PhRvA, 36, 2041
Janev, R. K., Belić, D. S., & Bransden, B. H. 1983, PhRvA, 28, 1293
Kallman, T., Bautista, M., Betancourt-Martinez, G., et al. 2019, BAAS, 51, 156
Kramida, A., Ralchenko, Y., Reader, J. & NIST ASD Team 2020, NIST Atomic Spectra Database (v5.7), https://physics.nist.gov/asd
Kuntz, K. D. 2018, A&ARv, 27, 1
Lallement, R. 2009, SSRv, 143, 427
Liang, G. Y., Zhu, X. L., Wei, H. G., et al. 2021, MNRAS, 508, 2194
Lisse, C., Christian, D., Wolk, S., et al. 2013, Icar, 222, 752
Liu, L., Wang, J. G., & Janev, R. K. 2014, PhRvA, 89, 012710
Lyons, D., Cumbee, R. S., & Stancil, P. C. 2017, ApJS, 232, 27
Machacek, J. R., Mahapatra, D. P., Schultz, D. R., et al. 2014, PhRvA, 90, 052708
Machacek, J. R., Mahapatra, D. P., Schultz, D. R., et al. 2015, ApJ, 809, 75
Minami, T., Pindzola, M. S., Lee, T.-G., & Schultz, D. R. 2006, JPhB, 39, 2877
Mullen, P. D., Cumbee, R. S., Lyons, D., & Stancil, P. C. 2016, ApJS, 224, 31
Olson, R. E. 1981, PhRvA, 24, 1726
Olson, R. E., & Salop, A. 1977, PhRvA, 16, 531
Pindzola, M. S., & Fogle, M. 2015, JPhB, 48, 205203
Pindzola, M. S., Fogle, M., & Stancil, P. C. 2018, JPhB, 51, 065204
Pindzola, M. S., & Schultz, D. R. 2008, PhRvA, 77, 014701
Popov, R. V., & Maiorova, A. V. 2017, OptSp, 122, 366
Rigazio, M., Kharchenko, V., & Dalgarno, A. 2002, PhRvA, 66, 064701
Seely, D. G., Andrianarijaona, V. M., Wulf, D., et al. 2017, PhRvA, 95, 052704
Simcic, J., Schultz, D. R., Mawhorter, R. J., et al. 2010a, ApJ, 722, 435
Simcic, J., Schultz, D. R., Mawhorter, R. J., et al. 2010b, PhRvA, 81, 062715
Smith, R., Kallman, T., Temi, P., et al. 2019, BAAS, 51, 110
Snios, B., Kharchenko, V., Lisse, C. M., et al. 2016, ApJ, 818, 199
Suraud, M. G., Hoekstra, R., de Heer, F. J., Bonnet, J. J., & Morgenstern, R. 1991, JPhB, 24, 2543
Zygelman, B., Cooper, D. L., Ford, M. J., et al. 1992, PhRvA, 46, 3846